Journal of Zhejiang University-SCIENCE A 2026 27(2):109-127
www.jzus.zju.edu.cn; www.springer.com/journal/11582
E-mail: jzus_a@zju.edu.cn

Research Article
https://doi.org/10.1631/jzus.A2400478

Check for updates

Finite element model updating methodology and application to flexible resonance of high-speed railway vehicles

Chao CHANG[1,2,3], Liang LING[2✉], Xiaoyi MA[1], Fansong LI[2], Tao LIU[3], Wanming ZHAI[2]

[1]*School of Mechatronics and Vehicle Engineering, East China Jiaotong University, Nanchang 330013, China*
[2]*State Key Laboratory of Rail Transit Vehicle System, Southwest Jiaotong University, Chengdu 610031, China*
[3]*CRRC Changchun Railway Vehicles Co., Ltd., Changchun 130062, China*

Abstract: The flexible resonance phenomenon of a carbody greatly affects the stability and safety of high-speed trains. Therefore, an accurate finite element (FE) model is crucial for establishing a rigid–flexible multi-body dynamics model and revealing the flexible resonance mechanism of high-speed trains. In this paper, we introduced an effective calibration and validation methodology for a carbody FE model of high-speed trains based on experimental modal analysis (EMA). A detailed three-dimensional (3D) carbody FE model that considered practical constraints was developed, and the carbody material parameters were optimized using a genetic algorithm (GA). Based on the updated model, a high-speed railway vehicle–track rigid–flexible coupled dynamics model was established. Results showed excellent agreement between the numerical simulations and field measurements. The proposed method was able to accurately reproduce the carbody flexible resonance phenomenon and elastic modal frequency observed on site.

Key words: High-speed train; Carbody flexible resonance; Finite element (FE); Model updating; Modal frequency

1 Introduction

The high-speed train (HST) has emerged as a highly effective mode of transport for journeys of medium to long distances, offering high levels of comfort, speed, and efficiency. As HSTs have increased in running speed, the need for lighter carbody structures has intensified, which can result in diminished stiffness and reduced frequencies of the lower-order elastic modes of the carbody. Concurrently, this rise in velocity has introduced several issues, including increased wheel–rail wear, reduced stability during operation, and heightened abnormal vibrations in the vehicles. The resonance phenomenon, particularly that caused by elastic deformation of the carbody, has been linked to decreased passenger comfort and compromised operational safety (Wei et al., 2017; Jing et al., 2021; Huang and Zeng, 2022). Moreover, the human body is highly perceptive to vertical vibrations within the range of 4–8 Hz, which coincides with the frequency band of abnormal resonances observed in the carriage (UIC, 1994).

To precisely capture the carbody's elastic deformation characteristics, the development of a dynamics model is essential, which necessitates the creation of an exceptionally precise finite element (FE) model. The practice of model updating is widely used across various disciplines such as structural health monitoring, aerospace, automotive, and civil engineering, to validate and refine the accuracy of FE models (Simoen et al., 2015; Chang et al., 2023). FE model updating constitutes a mathematical procedure where the initial model's assumptions and parameters are incrementally adjusted to achieve convergence. The main approach to FE model updating involves using experimental test data to ascertain the structural modal parameters, which are then compared with the model's predictions to facilitate the updating process. Typically, this involves the use of data such as acceleration time histories, frequency response functions (FRFs), natural frequencies, modal displacements, modal strains or curvatures, and modal deflections, all of which are

✉ Liang LING, liangling@swjtu.edu.cn
Chao CHANG, https://orcid.org/0000-0002-9671-6673

Received Oct. 16, 2024; Revision accepted Apr. 17, 2025;
Crosschecked Dec. 16, 2025; Online first Jan. 20, 2026

collected during experimental testing to inform the FE model updates (Alkayem et al., 2018).

However, FE model updating is a problematic and ill-conditioned inverse problem. Current FE model updating methods include sensitivity-based function methods (Rezaiee-Pajand et al., 2021; Zhu et al., 2021), Bayesian updating methods (Sadri et al., 2016; Ramancha et al., 2022), component mode synthesis techniques (Papadimitriou and Papadioti, 2013), response function methods (Arora, 2011), and a power spectral density (PSD) based strategy (Pedram et al., 2017). In recent years, more and more scholars have chosen to apply optimization algorithms to model updating. Several studies (Jung and Kim, 2013; Girardi et al., 2021; Xiong and Lian, 2021; Tran-Ngoc et al., 2022) adopted a global optimization algorithm to realize the modal modification of large structures. The research showed that an optimization algorithm has the advantages of strong adaptability, high search efficiency, and high accuracy.

Over recent decades, academics have proposed a variety of enhanced simulation models of tracks or infrastructures to analyze the vibration induced by wheel–rail interactions (Paixão et al., 2014; Malveiro et al., 2018). Modal identification and verification for railway bridges or tracks are based mainly on field measurements, using excitation methods such as impact loading (Ticona Melo et al., 2020), passing trains (Szafrański, 2021), or ambient excitation (Jiang et al., 2021). However, a vehicle system model allows more flexibility and can be used for both indoor experimental modal analysis (EMA) and outdoor operation modal analysis (OMA). Several studies (Ribeiro et al., 2021, 2022; Silva et al., 2021; Bragança et al., 2022) have described research on updating FE models of railway freight wagons. Compared with the results of freight wagon dynamic tests, an updated model has higher accuracy. The current model updating techniques have achieved good results for wagon models.

A passenger vehicle presents a significantly higher level of complexity and an expanded array of parameter variables than a wagon, which complicates the creation of an FE model that accurately mirrors the actual structure. Despite this, researchers have devised diverse strategies to tackle this difficulty. Using a particle swarm optimization algorithm, genetic algorithms (GA), and data from indoor modal tests, Akiyama et al. (2020) and Ribeiro et al. (2013) crafted a simplified FE model with reduced mesh density and successfully updated the FE model for high-speed train carriages. You et al. (2022) proposed an updating method that relies on measured FRFs to modify an HST carbody FE model, incorporating a Kriging surrogate model with multi-objective functions for optimization and calibration with the revised parameter values. Molodova et al. (2014) and Montenegro et al. (2015) concentrated on enhancing a wheel–rail contact model for passenger vehicles to achieve greater precision in vehicle–track coupled dynamics and wheel–rail high-frequency interactions. Despite the advancements from these studies, the following limitations remain in the context of FE model updating for HST passenger carbodies.

The existing railway passenger carbody FE models are relatively simple, and it is difficult to reflect the local vibration characteristics of the carbody structure. For instance, when detailed observations of deformation patterns, orientations, and other dynamic characteristics of specific structural components, such as the underframe and side walls of the carbody, are required for a particular modal shape, simplified FE models typically fail to deliver sufficient accuracy.

HSTs generally have various types of equipment placed underneath the underframe, which are connected by means of elastic or rigid connections. The arrangement of equipment and the connection parameters have been shown to affect the modal results of the vehicle (Gong et al., 2019).

The engineering problem of abnormal elastic vibration of the carbody due to poor wheel–rail matching, deterioration of bogie suspension components, and wheel polygonization, presents significant challenges. Despite much research, a comprehensive mechanism for the theoretical simulation of this vibration phenomenon has yet to be developed. As a result, an updated carbody FE model has been applied only rarely in relevant scenarios (Shi and Wu, 2016; Sun et al., 2021).

The aim of this study was to develop an effective calibration and validation method for a carbody FE model of HSTs based on EMA to establish a rigid–flexible multi-body dynamics model and reveal the flexible resonance mechanism of HSTs. We aimed to accurately reproduce the carbody flexible resonance phenomenon and elastic modal frequency observed on site. To achieve this goal, we set out to establish an accurate vehicle FE model by combining an optimization algorithm with modal test data.

The rest of this paper is structured as follows. The FE modelling of the HST carbody is presented in Section 2, which describes the numerical modelling technique in detail. In Section 3, we present the modal test on the carbody, including the test layout and parametric analysis. Section 4 shows the correction process of the model based on the GA and calibrates the accuracy of the model based on the modal assurance criterion (MAC) and frequency error indicators. An HST vehicle–track coupled dynamics model was constructed based on the updated carbody FE model, as detailed in Section 5. The carbody flexible vibration phenomena were reproduced for normal operation and resonance conditions. The findings and recommendations for additional research are presented in Section 6.

2 FE modelling of the HST carbody

2.1 Description of the HST carbody

This study focused on a new generation of Chinese passenger HSTs, operating at a maximum speed of 350 km/h. The HST features a distributed traction configuration comprising four motor vehicles and four trailers. Taking a trailer as an example, Fig. 1 shows a schematic diagram of the carbody. The carbody (trailer

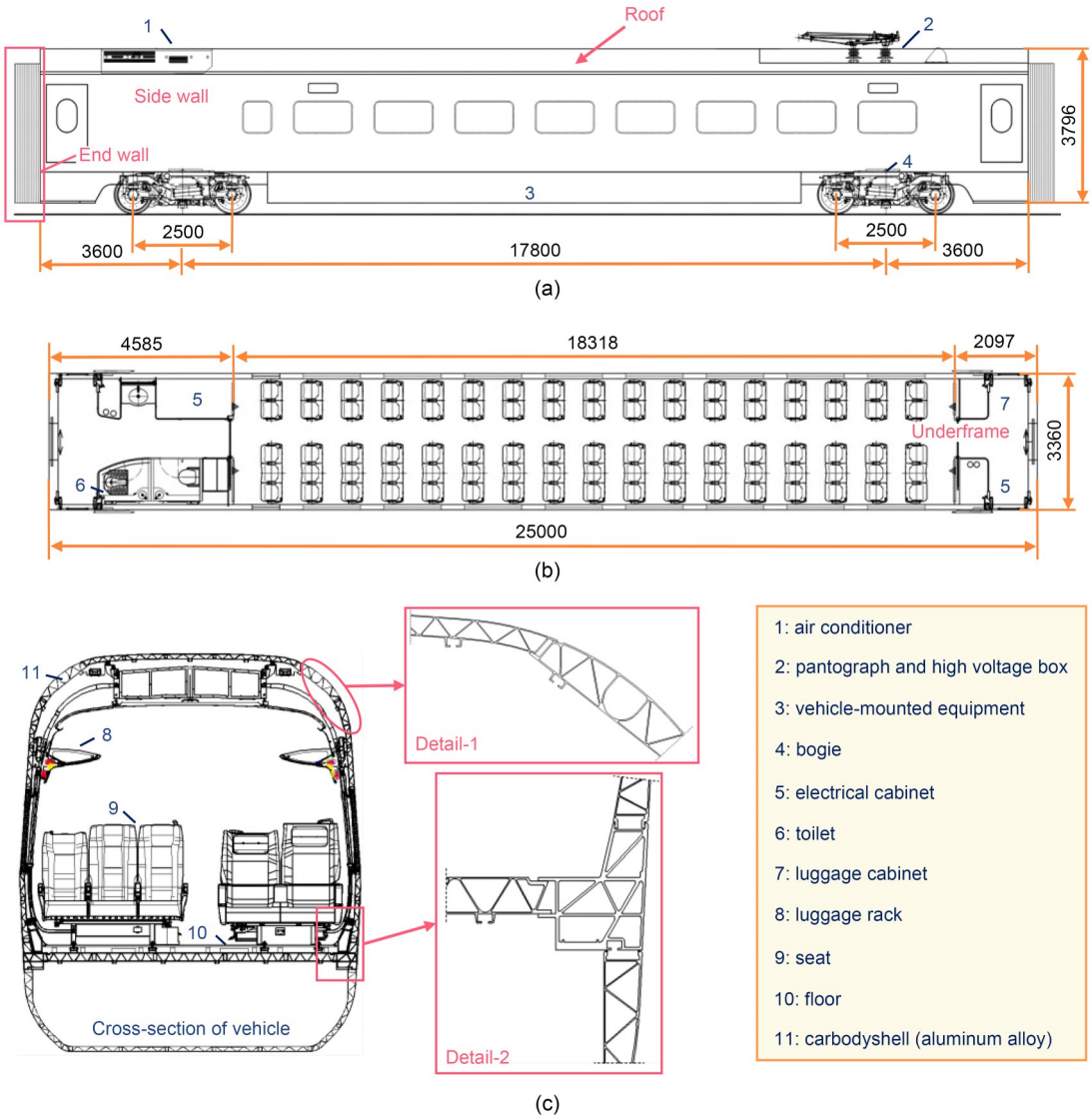

Fig. 1 Schematic diagram of an HST trailer carbody: (a) side view of vehicle (unit: mm); (b) interior layout of carriage (unit: mm); (c) cross-section and structural details

carriage) in service, including internal equipment, fittings, and other components, has a total mass of 41.03 t under no-load conditions and 45.89 t under normal load conditions. From both side and plan views (Figs. 1a and 1b), the length of the vehicle is 25.0 m, the wheelbase is 2.5 m, and the distance between the pivots of the bogies is 17.8 m. Fig. 1c shows the cross-section and structural details of the carbody.

As shown in Fig. 1, the carbody includes not only the aluminum alloy shell but also internal fittings and various equipment positioned underneath and inside. The carbody shell is made of large, hollow, and thin-walled aluminum alloy extrusion profiles that can be mechanically welded on a large scale.

Fig. 2 compares an actual photograph of the cabody shell with the fully equipped carbody in service. The fully equipped carbody weighs between 40 and 45 t, about four times heavier than the carbody shell (about 10 t). This significant difference is mainly due to the additional components that make up the carbody in service, which include equipment under the carbody weighing 5–10 t, an interior consisting of seats, windows, doors, luggage racks, and side wall panels weighing about 8 t, as well as other components such as the air conditioning system, equipment cabinets, cables, and toilet modules that collectively weigh about 10 t. Consequently, the modes of the carbody shell and the carbody in service exhibit stark contrasts. For example, the first modal frequency ($f_{mode,1}$) of the empty carbody shell was measured to be 13.03 Hz, whereas the carbody in service exhibited a frequency of 8.73 Hz, yielding a frequency difference of about 33%. Other modal orders showed similar significant differences.

Fig. 3 illustrates a schematic of the equipment installed under the carbody underframe. Fig. 3a shows the layout of the large-scale electrical and auxiliary equipment, whose mass varies from less than 1 t to several tons, and is situated under the underframe. The

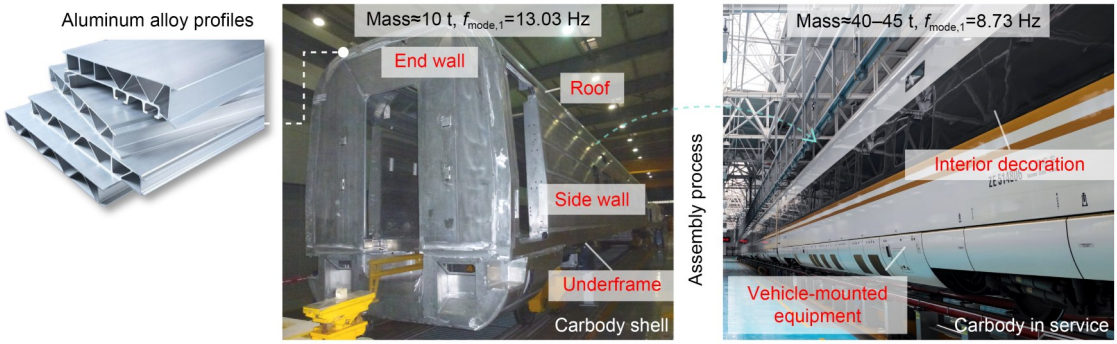

Fig. 2 Difference in appearance between the carbody shell and the carbody in service

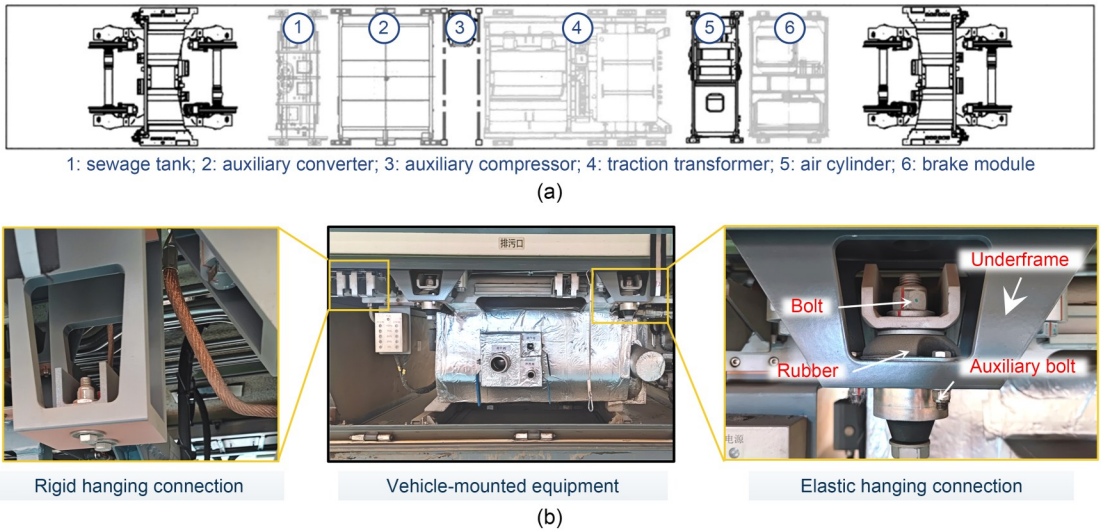

Fig. 3 Equipment under the carbody underframe: (a) equipment layout; (b) elastic hanging and rigid hanging connections

equipment includes a sewage tank, an auxiliary converter, an auxiliary compressor, a traction transformer, an air cylinder, and a braking module. The various items of equipment are connected to the side beams of the underframe through either elastic or rigid hanging mechanisms. Elastic hanging devices are supplemented with damping materials, whereas rigid suspensions are directly connected by bolts (Fig. 3b).

2.2 FE modelling of the HST carbody in service

Generally, an accurate model of a carbody shell of an HST can be obtained by the FE method. However, because the carbody is extremely complicated in operational service, there is a need to establish a more realistic FE model. In this study, we describe a method of creating the initial FE model in HyperMesh software. It is a pre-processing software for FE calculation (Zhang et al., 2008).

As shown in Fig. 4a, in accordance with the existing methods (Li et al., 2021, 2022), any distributed weight (such as internals and cables) located near the carbody shell was represented using mass points that are attached to the structure. Additionally, any concentrated mass (such as large equipment) is hung on the carbody shell in a realistic connection mode. The FE model also incorporated the bogie bolsters and

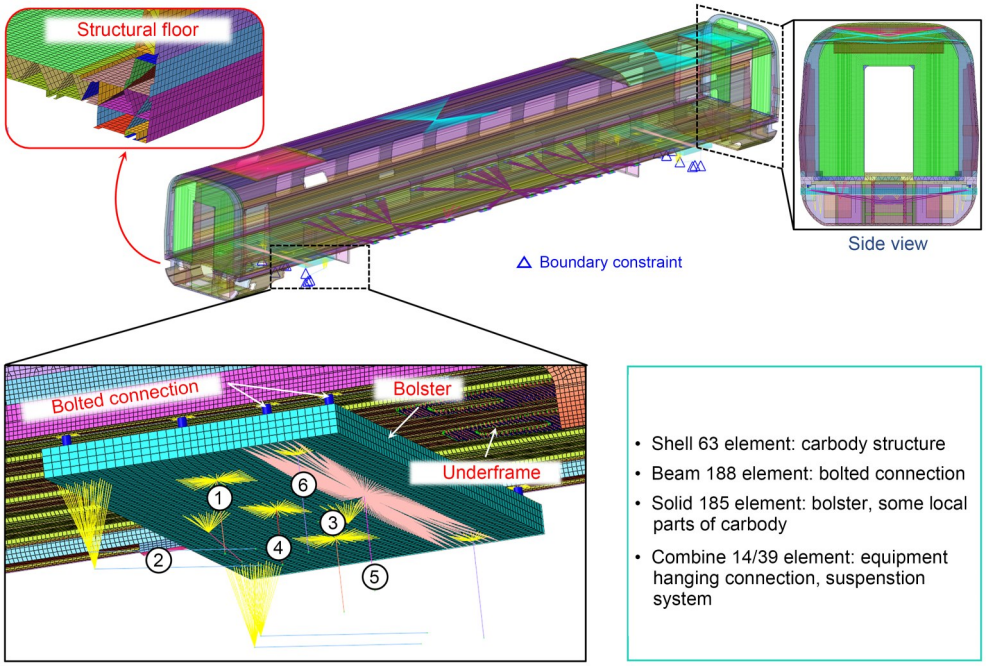

Fig. 4 Carbody FE model in operational service: (a) overall view and secondary suspension simulation; (b) FE simulation of on-board equipment, explicitly showing elastic and rigid connection details. References to color refer to the online version of this figure

secondary suspension devices, taking into account boundary constraints. For the bolster assembly, spring-damping elements (Combine 14/39 elements) were introduced to account for the properties of the air springs, anti-yaw dampers, anti-rolling torsion bars, and lateral dampers within the secondary suspension system. Particular attention was given to the representation of heavy and bulky equipment, such as traction converters or brake modules, mounted on the vehicle. In addition, in the process of building the carbody FE model, a mixed-element modelling strategy is adopted, wherein Shell 63 elements are utilized for the primary carbody structure, Beam 188 elements are employed to simulate bolted connections, and Solid 185 elements are applied for detailed modelling of the bolster and certain local structural components.

It is imperative to model elastic or rigid connections at the appropriate locations on the underframe or roof (Fig. 4b). In this study, Mass 21 elements were used to replicate the vehicle-mounted equipment, incorporating their mass and inertia characteristics. Rigid body element 3 (the object with linear distribution in Fig. 4) and Combine 14 elements were used to mimic the structural connections between the equipment. However, note that the shape of the equipment was not considered in the modelling process.

The model underwent a refinement process centered on the principle of equivalent stiffness (Li et al., 2022; Chang et al., 2023), accounting for the alterations in the carbody stiffness due to the presence of equipment and internal fittings. The carbody was segmented into four distinct zones according to the characteristics of the carbody shell structure: underframe, side walls, roof, and end walls. To emulate the increased stiffness contributed by doors and windows, coupling constraints were applied to these components. The carbody FE model was constructed with a total of 2420442 elements and 1958653 nodes, with Shell 63 elements dominating the composition. Note that the elastic modulus for the material in question was maintained as that of the aluminum alloy.

2.3 Modal analysis

Table 1 shows the material parameters of the carbody FE model before calibration. The initial material parameters were determined according to the carbody shell materials used in the manufacturing process. The first six modal shapes (Modes 1–6) and corresponding natural vibration frequencies (f_1–f_6) prior to any adjustments are illustrated in Fig. 5, calculated and solved by means of ANSYS software using the Lanczos method. Essentially, this method combines the vector inverse iteration and Rayleigh–Ritz methods to transform the initial eigenvalue problem into a more manageable tridiagonal matrix eigenvalue problem within the Ritz vector space, also referred to as the Lanczos vector space in this context (Paige, 1972).

Table 1 Parameters of the carbody FE model before calibration

Parameter	Value
Underframe's modulus, E_u (GPa)	71.0
Side wall's modulus, E_s (GPa)	71.0
Roof's modulus, E_r (GPa)	71.0
End wall's modulus, E_e (GPa)	71.0
Underframe's density, ρ_u (kg/m^3)	2700
Side wall's density, ρ_s (kg/m^3)	2700
Roof's density, ρ_r (kg/m^3)	2700
End wall's density, ρ_e (kg/m^3)	2700
Underframe's Poisson's ratio, μ_u	0.33
Side wall's Poisson's ratio, μ_s	0.33
Roof's Poisson's ratio, μ_r	0.33
End wall's Poisson's ratio, μ_e	0.33

The presented modes essentially involve global movements of the carbody, some of them also incorporating local movements of the carbody structure. Modes 1, 2, and 4 pertain to the bending vibration modes of the underframe of the vehicle, while Mode 3 is associated with the overall diamond vibration mode of the carbody. Mode 5 is related to the bending deformation of the underframe and the local deformation of the roof, while Mode 6 is focused on the torsional vibration mode of the carbody with simultaneous deformation of the underframe.

3 Modal test of the HST carbody

The objective of conducting a modal test on the operational HST carbody was to experimentally determine its modal parameters, which encompass the natural frequencies of vibration, corresponding mode shapes, and damping factors.

3.1 Measurement setup

The process of the modal test is shown in Fig. 6a. The carbody was supported on the bogies. The resolution of the accelerometer was 0.0001g rms (g is the

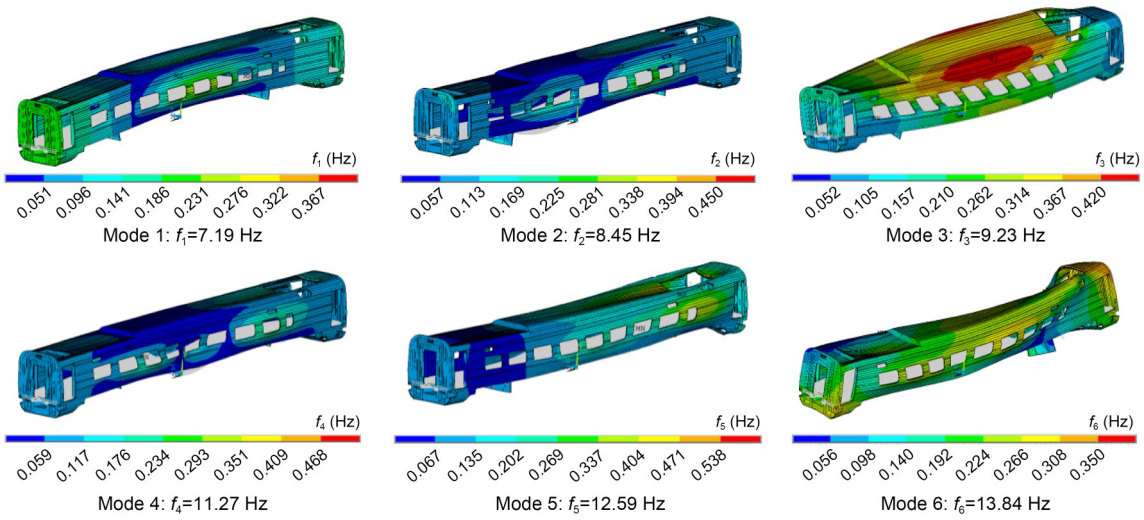

Fig. 5 Six modal shapes and corresponding natural vibration frequencies. References to color refer to the online version of this figure

gravitational acceleration; rms is the root mean square), and the sensitivity of the force sensor was 2.2 mV/N. The excitation force applied in the modal test was provided by an electric vibration exciter capable of generating burst random signals. The excitation force amplitude was controlled to ensure a stable and broadband excitation in the frequency range of interest (0–64 Hz). The exciter applied excitation at two carefully selected points on the carbody floor structure, chosen to avoid modal node locations. Analysis bandwidth was also 0–64 Hz, the number of spectral lines was 1024, and frequency resolution was 0.0625 Hz. The force signal source was burst randomly.

In addition, the reciprocity test needs to be completed. Select two excitation points, concentrating on the hard skeleton position of the carbody floor. Reciprocity testing in modal analysis is essential to verify the consistency and reliability of the measured FRF. In the measurement of the two-input multiple-output FRF, the self-power spectrum and the mutual power spectrum were used to calculate the FRF based on an average of 26 sampling times. The floor was flat, and there were no vibration sources in the vicinity.

The carbody was arranged with 196 measurement points. Fig. 6b shows the arrangement of the measurement points for the modal test, with the direction of the measurement points defined by the carbody coordinate system. In the test, the *XYZ* coordinate system was defined, where *X*-axis is the longitudinal direction of the carbody, *Y*-axis is the transverse direction of the carbody, and *Z*-axis is the vertical direction of the carbody. The modal experimental data were obtained by moving the accelerometers. There are 14 accelerometers within a single section. As the carbody structure is made up of the main frame structure and individual panels, the principle of the measurement points arrangement was divided into two parts. The first part was on the main carbody frame and the bottom longitudinal beam of the carbody. The second part was on each main panel, floor, and roof.

3.2 Modal parameter identification

The modal parameters for the carbody were identified by the application of the PolyMAX method implemented in the LMS software. The theoretical basis of the PolyMAX method is the least square complex frequency (LSCF) domain method (Peeters et al., 2004). The solving process is as follows: (1) the steady state diagram is determined by establishing a linear direct intersection matrix fractional model to determine the real modal frequency, damping, and participation factor (Eqs. (1)–(3)); (2) obtaining poles and modal participation factors (Eq. (4)); (3) least squares frequency domain (LSFD) method for modal analysis (Eq. (5)).

$$\boldsymbol{H}(w)=\boldsymbol{B}(w)\,\boldsymbol{A}(w)^{-1}, \tag{1}$$

$$\begin{cases}\boldsymbol{B}(w)=\sum_{r=0}^{p}\boldsymbol{Z}(w)^{r}\boldsymbol{\beta}_r,\\ \boldsymbol{A}(w)=\sum_{r=0}^{p}\boldsymbol{Z}(w)^{r}\boldsymbol{\alpha}_r,\end{cases} \tag{2}$$

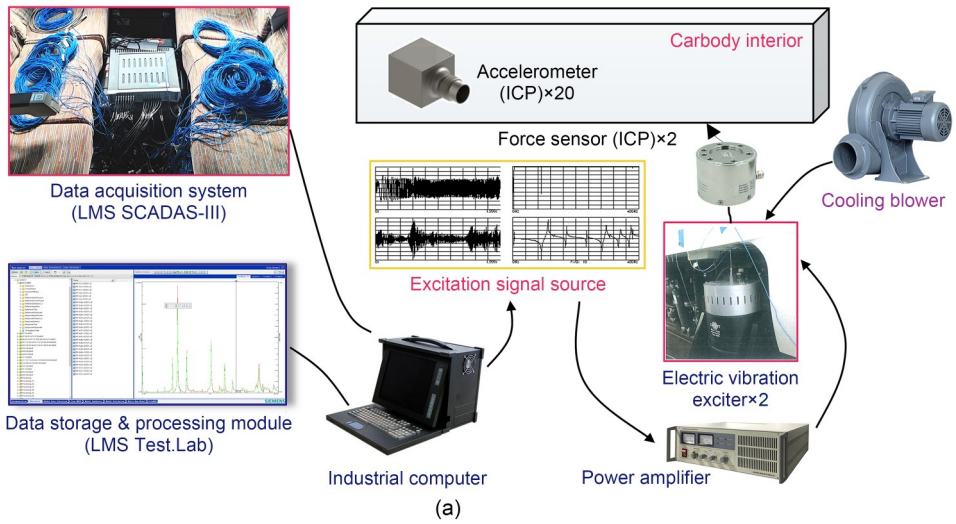

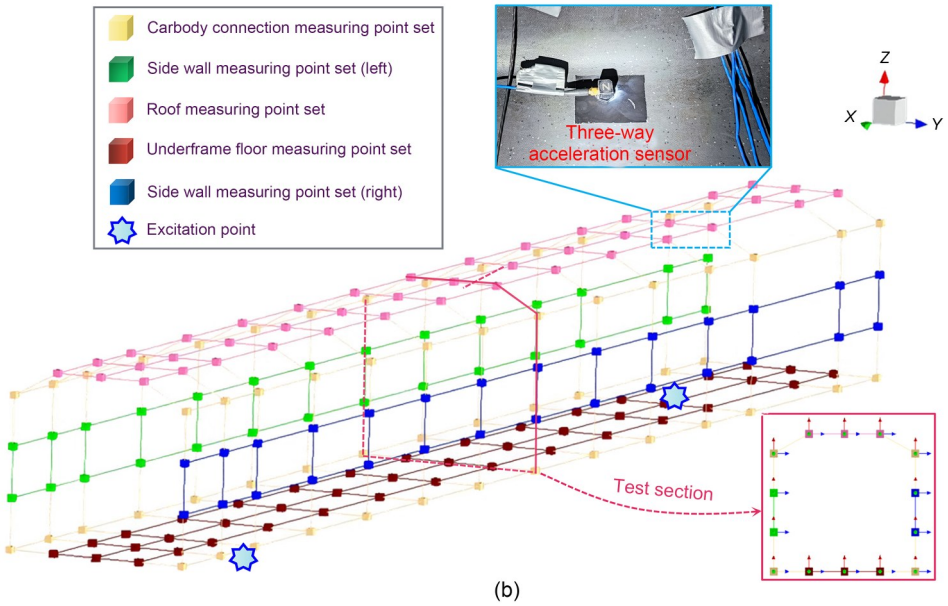

Fig. 6 (a) Flowchart of the carbody modal test; (b) layout of measuring points. LMS SCADAS-III is the data acquisition hardware system; LMS Test.Lab is the integrated testing and analysis software platform; ICP indicates that the type of the sensor is integrated circuit piezoelectric. References to color refer to the online version of this figure

where w is the modal nature frequency; $\boldsymbol{H}(w)$ is the FRF; $\boldsymbol{B}(w)$ is the output parameter channel matrix; $\boldsymbol{A}(w)$ is the input parameter channel matrix; $\boldsymbol{\alpha}_r$ and $\boldsymbol{\beta}_r$ (r=0, 1, ⋯, p) are the polynomial coefficients of the numerator and denominator matrix, respectively; p is the order of the mathematical model, which reflects the complexity of the model; $\boldsymbol{Z}(w)$ is the elementary item of the polynomial, which can be expressed as:

$$\boldsymbol{Z}(w)=\mathrm{e}^{-\mathrm{j}w\Delta t}, \tag{3}$$

where j is the imaginary unit; Δt is the sampling time.

$$\begin{bmatrix} \boldsymbol{O} & \boldsymbol{I} & \boldsymbol{O} & \cdots & \boldsymbol{O} \\ \boldsymbol{O} & \boldsymbol{O} & \boldsymbol{I} & \cdots & \boldsymbol{O} \\ \vdots & \vdots & \vdots & \ddots & \vdots \\ -\boldsymbol{\alpha}_0 & -\boldsymbol{\alpha}_1 & -\boldsymbol{\alpha}_2 & \cdots & -\boldsymbol{\alpha}_{p-1} \end{bmatrix} \times \begin{bmatrix} \boldsymbol{V} \\ \boldsymbol{\Lambda V} \\ \boldsymbol{\Lambda}^2\boldsymbol{V} \\ \vdots \\ \boldsymbol{\Lambda}^p\boldsymbol{V} \end{bmatrix} = \begin{bmatrix} \boldsymbol{O} \\ \boldsymbol{O} \\ \vdots \\ \boldsymbol{O} \end{bmatrix}, \tag{4}$$

where $\boldsymbol{O}$ is the zero matrix; $\boldsymbol{I}$ is the identity matrix; $\boldsymbol{\Lambda}$ is the eigenvalue matrix (diagonal matrix); $\boldsymbol{V}$ is the eigenvector matrix.

$$\boldsymbol{H}(w)=\sum_{i=1}^{N}\left[\frac{\boldsymbol{\psi}_i\boldsymbol{l}_i^{\mathrm{T}}}{\mathrm{j}w-\boldsymbol{\lambda}_i}+\frac{\boldsymbol{\psi}_i^{*}\boldsymbol{l}_i^{\mathrm{T}}}{\mathrm{j}w-\boldsymbol{\lambda}_i^{*}}\right]-\frac{\boldsymbol{R}_{\mathrm{L}}}{w^2}+\boldsymbol{R}_{\mathrm{U}}, \quad (5)$$

where N is the number of modes; $\boldsymbol{\psi}_i$ (i=1, 2, ⋯, N) is the ith-order modal vibration mode; $\boldsymbol{l}_i$ is the ith-order modal participation factor; $\boldsymbol{\lambda}_i$ is the ith-order modal pole; $\boldsymbol{\psi}_i^{*}$ and $\boldsymbol{\lambda}_i^{*}$ are the complex conjugate transposes of $\boldsymbol{\psi}_i$ and $\boldsymbol{\lambda}_i$, respectively; $\boldsymbol{R}_{\mathrm{L}}$ and $\boldsymbol{R}_{\mathrm{U}}$ are the lower and upper residual items, respectively.

The FRF data were selected based on clear FRFs and coherence close to 1 in the test frequency band. The parameter estimation frequency range was chosen within this band, with no more than 10 system poles. To minimize out-of-band effects, the start and end points of the selected frequency band were set to the minimum values. When estimating the number of poles, the measured FRFs of the selected points were summed by amplitude. Modal model verification first checks the exciter's fixation, sensor calibration, and signal quality. The obtained FRFs are verified by coherence, then compared with the reconstructed FRFs from modal parameter estimation in LMS software, considering the upper and lower residuals.

The second step was to determine the correctness of each estimate in the same group according to the MAC indicator. The MAC indicator evaluates the spatial intersection of the two modes by evaluating the size of the elements on the non-diagonal line. In addition to the MAC indicator, we used the modal phase collinearity (MPC) indicator with the MAC indicator. The MPC indicator is a measure of the degree to which the modal phases of the measured responses at different points on a structure are collinear or aligned with each other (Carne and Dohrmann, 1995). The MPC can be used to evaluate the consistency of the measured modal parameters across different measurement locations. Both MPC and MAC indicators are important for ensuring the rationality of modal testing and should be used together to provide a more comprehensive evaluation of the modal testing results.

MAC indicator $M_{\mathrm{AC}}(\boldsymbol{\psi}_k^m, \boldsymbol{\psi}_l^m)$ expresses the correlation between modal shape vectors $\boldsymbol{\psi}_k^m$ and $\boldsymbol{\psi}_l^m$, and the expression is as follows:

$$M_{\mathrm{AC}}(\boldsymbol{\psi}_k^m, \boldsymbol{\psi}_l^m)=\frac{\left|(\boldsymbol{\psi}_k^m)^{*}\boldsymbol{\psi}_l^m\right|^2}{\left((\boldsymbol{\psi}_k^m)^{*}\boldsymbol{\psi}_k^m\right)\left((\boldsymbol{\psi}_l^m)^{*}\boldsymbol{\psi}_l^m\right)}, \quad k\neq l, \quad (6)$$

where $\boldsymbol{\psi}_k^m$ and $\boldsymbol{\psi}_l^m$ are the modal shape vectors of the kth- and lth-order modal vibration mode, respectively; m is the order of the mode; $(\boldsymbol{\psi}_k^m)^{*}$ and $(\boldsymbol{\psi}_l^m)^{*}$ are the complex conjugate transposes of $\boldsymbol{\psi}_k^m$ and $\boldsymbol{\psi}_l^m$, respectively. The more linearly the two sets of vectors $(\boldsymbol{\psi}_k^m, \boldsymbol{\psi}_l^m)$ are related, the closer the MAC indicator is to 1, which indicates that the kth measured mode shape is the same as the lth measured mode shape; otherwise, the lower the correlation.

The MPC indicator is the linear relationship between the real part and the imaginary part of each element of the mode vector of the scaleless mode. For the real regular mode, the MPC indicator should have a high value, usually close to 100%. The MPC indicator $M_{\mathrm{PC}}(\tilde{\boldsymbol{\psi}}_k)$ of the modal shape vector $\tilde{\boldsymbol{\psi}}_k$ can be calculated by Eqs. (7)–(9) (Reynders et al., 2012):

$$M_{\mathrm{PC}}(\tilde{\boldsymbol{\psi}}_k)=\frac{\left\|\mathrm{Re}(\tilde{\boldsymbol{\psi}}_k)\right\|_2^2}{\left\|\mathrm{Re}(\tilde{\boldsymbol{\psi}}_k)\right\|_2^2+\left\|\mathrm{Im}(\tilde{\boldsymbol{\psi}}_k)\right\|_2^2}+\frac{\dfrac{1}{\varsigma_{\mathrm{MPC}}}\mathrm{Re}(\tilde{\boldsymbol{\psi}}_k^{\mathrm{T}})\mathrm{Im}(\tilde{\boldsymbol{\psi}}_k)[2(\varsigma_{\mathrm{MPC}}^2+1)\sin^2(\theta_{\mathrm{MPC}})-1]}{\left\|\mathrm{Re}(\tilde{\boldsymbol{\psi}}_k)\right\|_2^2+\left\|\mathrm{Im}(\tilde{\boldsymbol{\psi}}_k)\right\|_2^2}, \quad (7)$$

$$\varsigma_{\mathrm{MPC}}=\frac{\left\|\mathrm{Im}(\tilde{\boldsymbol{\psi}}_k)\right\|_2^2-\left\|\mathrm{Re}(\tilde{\boldsymbol{\psi}}_k)\right\|_2^2}{2\mathrm{Re}(\tilde{\boldsymbol{\psi}}_k)\mathrm{Im}(\tilde{\boldsymbol{\psi}}_k)}, \quad (8)$$

$$\theta_{\mathrm{MPC}}=\arctan\left[|\varsigma_{\mathrm{MPC}}|+\mathrm{sign}(\varsigma_{\mathrm{MPC}})\sqrt{1+\varsigma_{\mathrm{MPC}}^2}\right], \quad (9)$$

where $\tilde{\boldsymbol{\psi}}_k$ is the kth-order modal shape vector obtained by experimental measurement; ς_{MPC} is the normalization factor in the MPC indicator formulation; θ_{MPC} is the phase angle associated with the MPC indicator.

After carrying out a thorough analysis and observation of the vibration mode, we were able to determine the effective mode model for the project. The MAC and MPC indicator values obtained from the modal test (Figs. 7a and 7b, respectively) were compared against engineering standards. The MAC indicator was considered relevant if greater than 0.7 and irrelevant if less than 0.1. Off-diagonal terms in the MAC indicator matrix were observed to be less than 0.1, satisfying the discrimination criterion. Similarly, the MPC

indicator had to be above 90%, which was met by the test results. To select the appropriate excitation points for the carbody, we carried out pre-tests and compared the results obtained from different points. Reciprocity tests were then conducted. Fig. 7c shows a comparison of the *Z*-direction frequency response functions of the excitation point 2 (H_2) when excitation point 1 (H_1) is excited and the H_1 measuring point when H_2 is excited. These results met the reciprocity requirements.

Fig. 8a presents the full FRFs at the observation point, enabling the distinct identification of the frequency associated with the carbody overall vibration mode. Fig. 8b shows the configurations of six identified vibration modes of the carbody, showcasing the

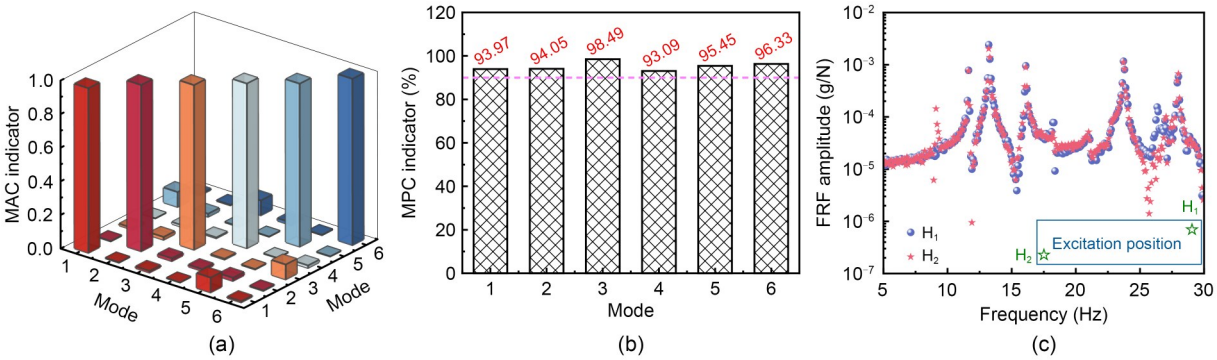

Fig. 7 Verification and analysis of modal test results: (a) MAC indicator; (b) MPC indicator; (c) reciprocity test of excitation points

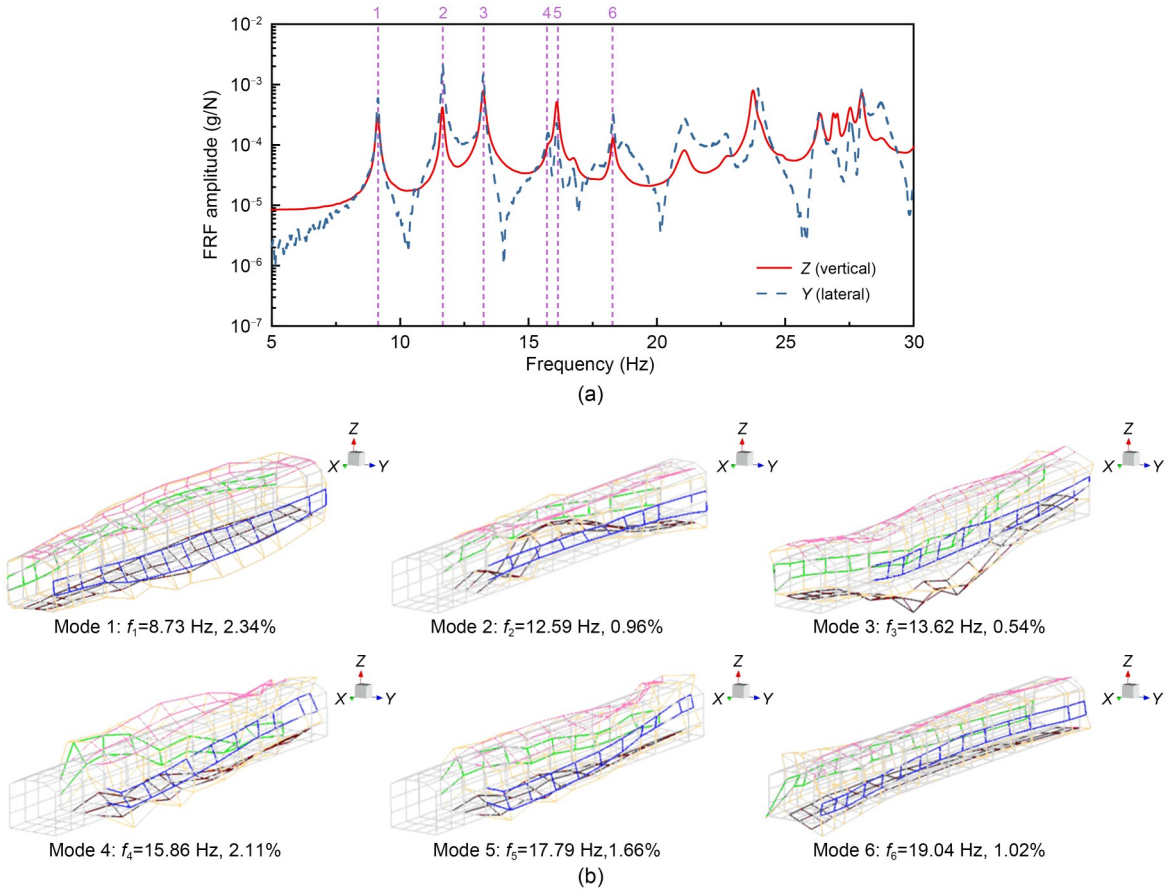

Fig. 8 (a) Identified modal parameters; (b) experimental modal shapes of the carbody with corresponding modal natural frequencies and damping ratios. References to color refer to the online version of this figure

mean values for natural frequencies and damping ratios. The deformed modal shapes are depicted with colored lines, while the undeformed mesh is shown in grey.

Mode 1 corresponds to the carbody first-order diamond vibration mode. Mode 2 represents the first-order bending of both the floor and roof. Mode 3 is characterized by the first-order vertical bending of the entire carbody. Mode 4 involves the second-order lateral bending of the underframe and roof, in conjunction with the second-order vertical side wall bending. Mode 5 is a combination of the first-order torsion and the first-order lateral bending. Mode 6 comprises the second-order torsion and the second-order lateral bending. The modal shape diagrams clearly show that the original and uncorrected carbody FE models significantly deviate from the experimental results, highlighting the need to refine the model.

4 Calibration of the carbody FE model

Section 4 describes how the refinement of the HST carbody FE model was carried out using the outcomes from the modal test, incorporating a sensitivity analysis and an optimization process that used a GA. The numerical and experimental mode shapes were automatically matched using the MAC indicator, facilitating a comparative correlation analysis of the derived modal parameters.

4.1 Sensitivity analysis

A sensitivity analysis allows for the selection of the numerical parameters (i.e., six natural frequencies (f_1–f_6) and six MAC indicators (MAC 1–MAC 6)) that most influence the modal responses and should be included in the subsequent optimization stage. Twelve numerical parameters in Table 1 were selected, and random sampling was carried out using the Latin hypercube sampling (LHS) method (Helton and Davis, 2003). LHS is a statistical technique used to generate a set of samples that are uniformly distributed over a specified range of values. The HyperMesh software completes the carbody FE model in service. According to Section 2, each region was given different material properties, accompanied by two bogie systems. The output was an ANSYS-readable ".cdb" format file, and ANSYS software was used for modal analysis.

In the optimization process, only those parameters that are significantly correlated with the response can be correctly estimated. This can minimize the amount of calculation. The sensitivity analysis results are based on the Spearman correlation coefficient r_{xy}^{S}, which expresses the correlation between two vectors of samples, $\boldsymbol{x}$ and $\boldsymbol{y}$, based on their rank order vectors, $R(\boldsymbol{x}_i)$ and $R(\boldsymbol{y}_i)$ (Silva et al., 2016):

$$r_{xy}^{\mathrm{S}}=\frac{\sum_{i=1}^{n}[R(\boldsymbol{x}_i)-\bar{R}_x][R(\boldsymbol{y}_i)-\bar{R}_y]}{\sqrt{\sum_{i=1}^{n}[R(\boldsymbol{x}_i)-\bar{R}_x]^2\sum_{i=1}^{n}[R(\boldsymbol{y}_i)-\bar{R}_y]^2}}, \quad (10)$$

where $\bar{R}_x$ and $\bar{R}_y$ are the average values of the rank-order vectors $R(\boldsymbol{x}_i)$ and $R(\boldsymbol{y}_i)$, respectively, with i=1, 2, ⋯, n, where n is the number of samples of each vector.

Fig. 9 shows the global sensitivity analysis results of 500 samples, based on the Spearman linear correlation matrix. To ensure the correct identification of parameters that have a significant impact on the modal response, samples with a MAC indicator value

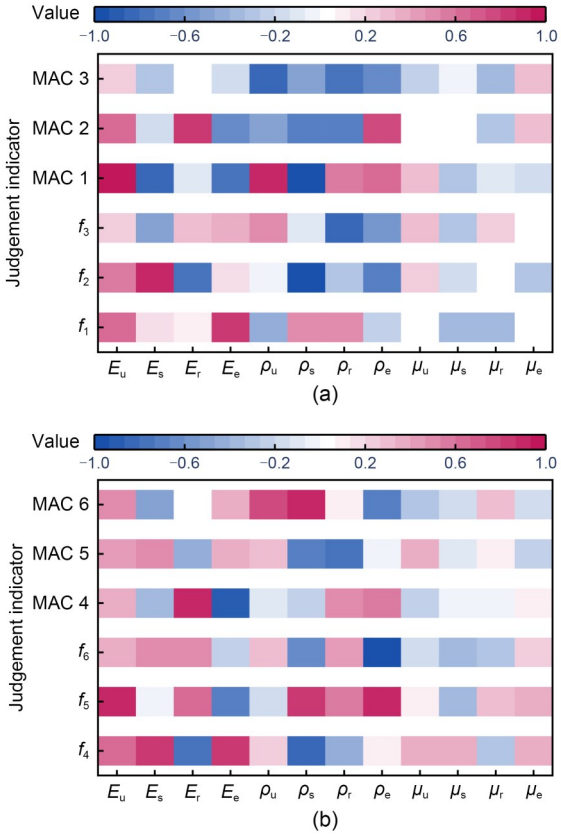

Fig. 9 Parameter sensitivity analysis: (a) MAC 1–MAC 3 and f_1–f_3; (b) MAC 4–MAC 6 and f_4–f_6. References to color refer to the online version of this figure

below 0.50 were excluded from the total number of samples. This strategy proved effective in filtering out irrelevant samples. Continuing with the optimization stage, we considered only those parameters with a Spearman correlation coefficient above 0.50 that were associated with the modal response. The results of the sensitivity analysis show that the elastic moduli (i.e., E_u, E_s, E_r, E_c) and density parameters (i.e., ρ_u, ρ_s, ρ_r, ρ_c) of four regions, namely the underframe, the side wall, the roof, and the end wall, were prominent in the modal response, while the Poisson's ratio had little effect.

4.2 Modal parameter optimization

The main objective of optimization is to determine the optimal value of a set of parameters identified through sensitivity analysis, to reduce the differences between simulation results and experimental results. To achieve this, a numerical model optimization process was initiated using a GA that requires the integration of two software packages, ANSYS and MATLAB. GA is an adaptive global optimization search algorithm, which simulates the process of biological heredity and evolution.

Fig. 10 outlines the iterative approach for updating the FE model. The GA was implemented within the MATLAB software framework, which interfaced with ".cdb" files for conducting numerical simulations to assess natural frequencies and mode shapes. ANSYS-generated modal analysis data were transferred to MATLAB for modal pairing, where each experimental mode was matched with its numerical counterpart based on the highest MAC indicator value. The GA then estimated a new set of numerical parameters with the goal of reducing the residuals of the objective function. This iterative cycle was repeated until the predefined iteration limit was achieved. For the purposes of this research, binary coding was used, along with an initial population size of 50, a maximum evolutionary algebra of 50, and a generation gap of 0.9. The uniform crossover method was used, setting the crossover probability at 0.7 and the mutation probability at 0.05. The initial population was generated at random using LHS method.

The upper and lower limits of the equivalent elastic moduli of the four regions are listed in Table 2, with their values set at 30 and 150 GPa, respectively,

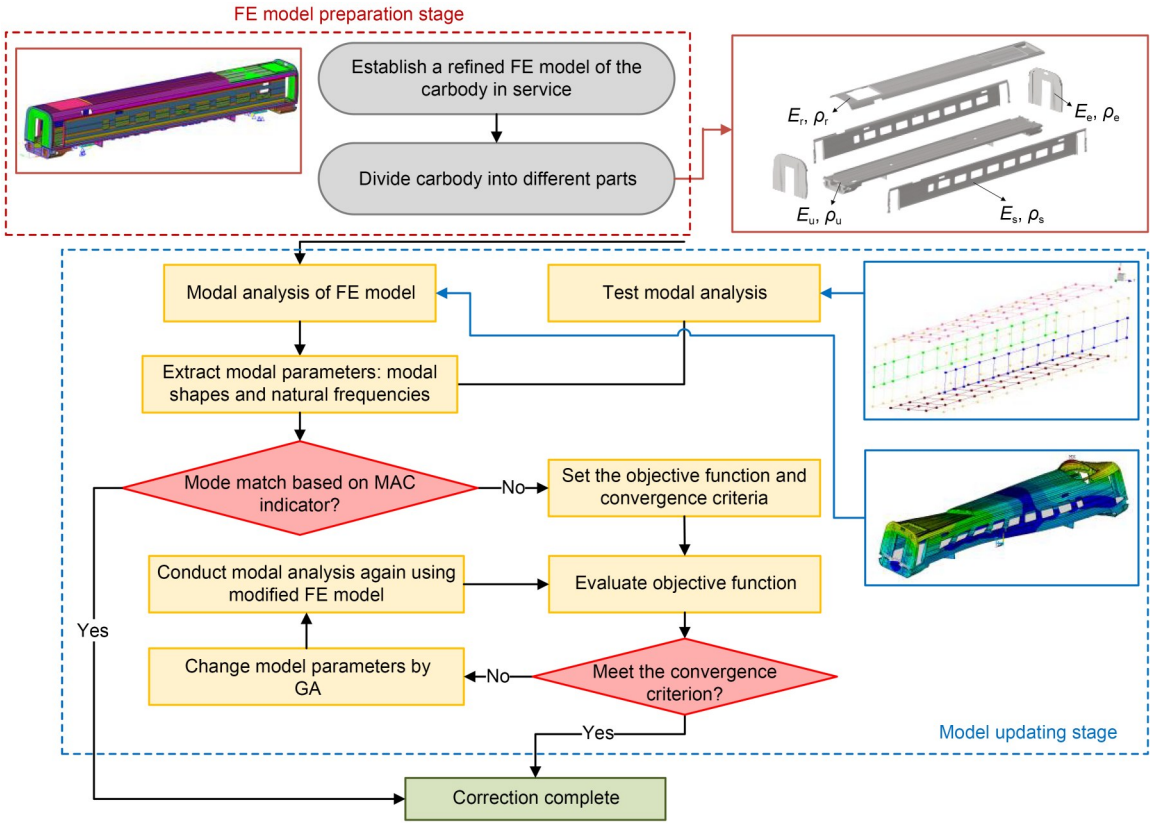

Fig. 10 FE model updating process used in this study

Table 2 Parameters considered in the optimization analysis

Parameter	Initial value	Value range
Underframe's modulus, E_u (GPa)	71.0	30–150
Side wall's modulus, E_s (GPa)	71.0	30–150
Roof's modulus, E_r (GPa)	71.0	30–150
End wall's modulus, E_e (GPa)	71.0	30–150
Underframe's density, ρ_u (kg/m^3)	2700	1000–10000
Side wall's density, ρ_s (kg/m^3)	2700	1000–10000
Roof's density, ρ_r (kg/m^3)	2700	1000–10000
End wall's density, ρ_e (kg/m^3)	2700	1000–10000

to enable the GA to search for an optimal solution across a broad range (Li et al., 2022). Limits were also set when individual values within the population were updated and when these values exceeded the imposed limits. In reference to the optimization results, the density range of the four regions was set within 1000–10000 kg/m^3 to guarantee sufficient coverage during the search process.

The objective function f includes two terms: one is related to the natural frequencies of global and local modes, and the other is related to the MAC indicator of global and local mode shapes:

$$f=\frac{100\alpha}{\sum_{i=1}^{I}\gamma_i}\sum_{i=1}^{I}(\gamma_i|\Delta f_i|)+\frac{100\beta}{n}\sum_{i=1}^{I}(1-M_{\mathrm{AC}}(\boldsymbol{\psi}_i^{\mathrm{a}},\boldsymbol{\psi}_i^{\mathrm{t}})), \tag{11}$$

$$\Delta f_i=\frac{f_i^{\mathrm{t}}-f_i^{\mathrm{a}}}{f_i^{\mathrm{t}}}, \tag{12}$$

where $M_{\mathrm{AC}}(\psi_i^{\mathrm{a}},\psi_i^{\mathrm{t}})$ (i=1, 2, ⋯, I) is the MAC indicator between $\boldsymbol{\psi}_i^{\mathrm{a}}$ and $\boldsymbol{\psi}_i^{\mathrm{t}}$, which quantifies the morphological consistency of the two modal shapes; I is the number of modes to be corrected; $\boldsymbol{\psi}_i^{\mathrm{a}}$ is the ith analytical modal shape obtained from the FE analysis; $\boldsymbol{\psi}_i^{\mathrm{t}}$ is the ith experimental modal shape measured via experimental method; α is the weight factor of the modal frequency and experimental modal frequency error; β is the weight factor of the modal shape correction part. To distinguish the degree of participation of each mode in iterative calculation, a parameter γ_i is added to the equation, which represents the weight factor of the ith mode, with a value ranging from 0 to 1. For the mode order that is the key correction, the mode weight factor was 1. Δf_i is the relative deviation of the modal frequency of the ith model; f_i^{t} is the experimental modal frequency of the ith mode; f_i^{a} is the analytical modal frequency of the ith mode.

In Eq. (11), the first part on the right-hand side aims to match the natural frequency of the model to that of the test as closely as possible. The second part modifies the model's modal function matrix. Research shows that the value of α/β within the range of 2 to 10 yields satisfactory correction results. In this study, the value was set to 4, with an α value of 1.00 and a β value of 0.25. As a result, the convergence judgment value of the objective function f was typically 4.50 for each mode represented in Eq. (12). Fig. 11 presents the relationship between the number of iterations and the evaluation function value. As the population evolves to the 30th generation, the evaluation function under the optimal value gradually approaches the objective function value of 4.50.

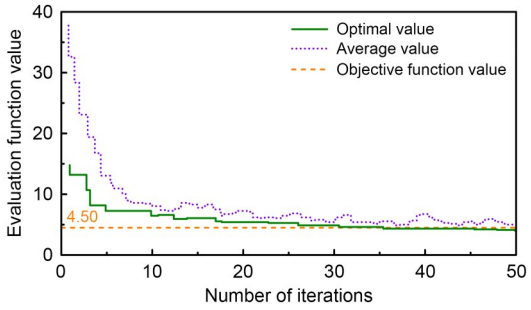

Fig. 11 Evaluation function value versus iterations during GA optimization

The determined material parameters were as follows: E_u=112.0 GPa, E_r=55.2 GPa, E_s=66.4 GPa, and E_e=65.7 GPa. Notably, the equivalent elastic modulus for certain areas did not exceed the characteristic elastic modulus of aluminum alloy (69.0 GPa), with numerous sites exhibiting lower elastic moduli. The value of E_u exceeded 69.0 GPa, suggesting that the internal structure of the carbody enhances its operational stiffness. In contrast, the values of E_r, E_s, and E_e, which were below 69.0 GPa, denote a reduction in stiffness in these specific sections. The final optimization result of the density parameters was updated as follows: ρ_u=9029.3 kg/m^3, ρ_s=6566.7 kg/m^3, ρ_r=7076.9 kg/m^3, and ρ_e=5175.1 kg/m^3.

Fig. 12a presents a comparison of the experimental and calibrated numerical modal configurations. A marked resemblance between the numerical and experimental configurations was realized post-calibration. As shown in Figs. 12b and 12c, the MAC indicator values were all greater than 0.8, and the absolute value

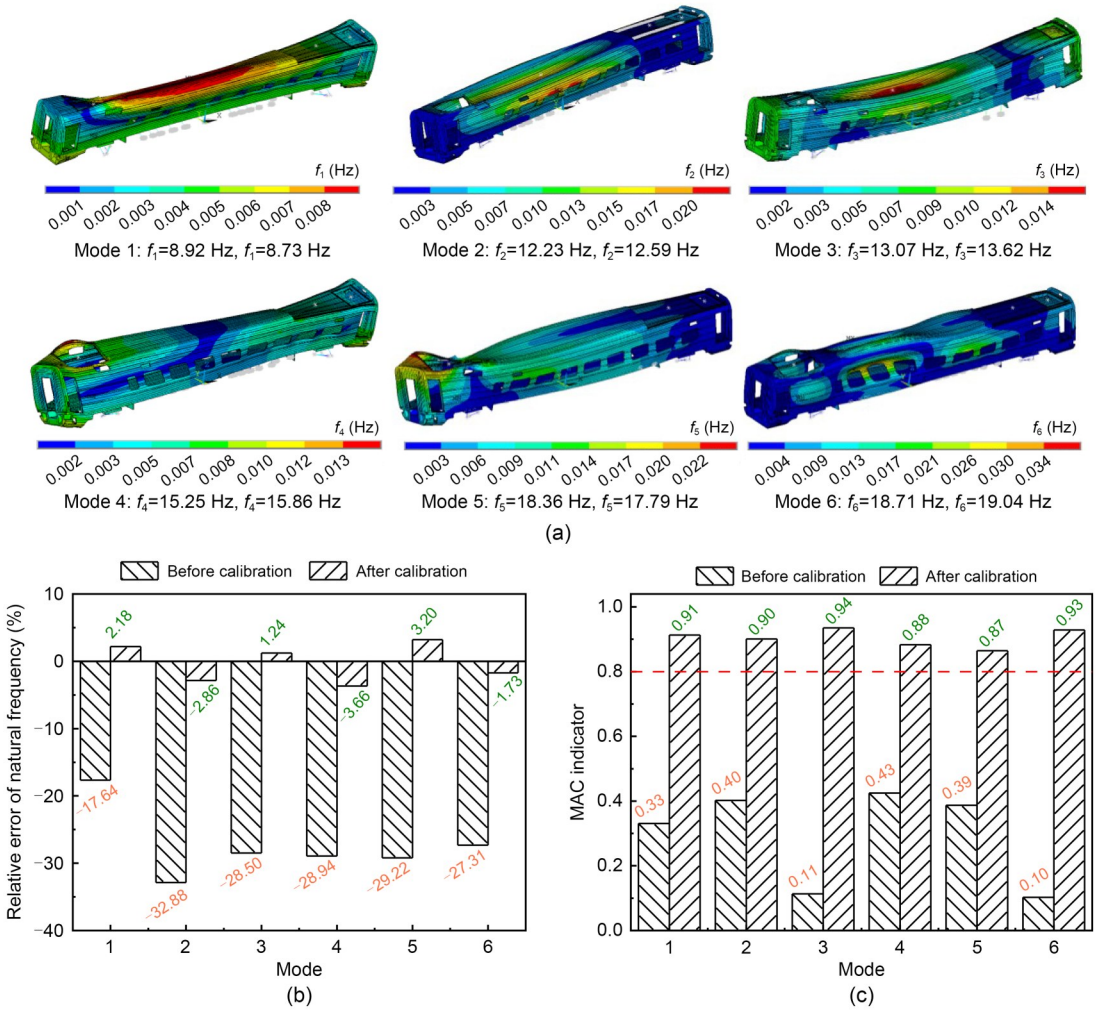

Fig. 12 (a) Comparison of modal natural frequencies between the experimental (left value) and numerical (right value) simulation as well as modal shapes after FE model updating; (b) relative errors of natural frequency before and after calibration; (c) MAC indicator before and after calibration. References to color refer to the online version of this figure

of the relative error of each mode frequency was less than 5%. The accuracy of the updated FE model was obviously improved. Note that the prerequisite for revising the carbody FE model is to have experimental data as input, which is typically done after the initial product design is finalized. The updated model can then be used for fault identification, discussion of potential solutions, and optimization of the product design.

5 Application in the flexible resonance of a high-speed railway vehicle

Section 5 describes the application of the proposed model to the flexible resonance analysis of a high-speed railway vehicle. The dynamic responses obtained by the HST vehicle–track coupled model based on the updated carbody FE model, and the in-situ dynamic measurements are compared.

5.1 HST vehicle–track coupled model

The updated FE model was used to construct a rigid–flexible coupled dynamics model of the whole vehicle using both the vehicle–track coupled dynamics theory (Fig. 13) and Craig–Bampton modal synthesis method (Boo et al., 2018; Zhai, 2019). This vehicle system model comprises a flexible carbody, two bogies, five on-board pieces of equipment installed beneath the underframe, an air conditioning system on the roof, four wheelsets, two bolster beams, and eight axle boxes. The wheelset, frame, and other components with limited elastic deformation were treated as a rigid body.

The bolster and underframe were rigidly connected. Maxwell models were used to calculate damping forces in the suspension systems, and linear springs and dampers were used to mimic air springs and tailored elements to represent rubber components and bearings.

The dynamics of a slab ballastless track were treated as an object. The modelling of the track was based on the vibration theory of an elastic thin plate, described in detail by Zhai (2019). The rail was simplified to a Timoshenko beam element. A full nonlinear non-Hertz Kik–Piotrowski model for wheel–rail normal contact was hired. It is a non-elliptical multipoint contact model based on the virtual penetration contact theory (Piotrowski and Kik, 2008). The fast simulation algorithm was used to calculate the tangential stress distribution in the contact patch, and the wheel–rail tangential force was obtained by integration (Kalker, 1967, 1982; Sun et al., 2023).

5.2 Simulation of the flexible resonance of the high-speed vehicle

Fig. 14 shows an abnormal condition of the ride comfort index in the middle floor of the vehicle carbody during a certain operation, with a maximum operation speed of 350 km/h. In this study, based on the work of Zhai (2019), the Sperling index was selected for assessing ride comfort. When the Sperling index is greater than 3.00, it is considered unqualified. The vertical and lateral Sperling indices exceeded the qualified line many times during operation, especially the vertical index, which had a maximum value of 3.93.

According to the feedback from the in-situ test, in the time period when the Sperling index was abnormal, foot numbness can be obviously felt in the middle of the carbody floor, accompanied by the vibration phenomenon inside the carriage. The carbody shaking phenomenon appears to be similar to that described previously (Shi and Wu, 2016; Wei et al., 2017; Huang and Zeng, 2022) and may be caused by wheel–rail profile matching, abnormal disturbance of track irregularity in local areas, and other factors (Polach and Nicklisch, 2016; Chen et al., 2023; Hu et al., 2025).

Fig. 15 shows the simulation analyses of normal operation and carbody shaking condition based on the rigid–flexible coupled dynamics model, with the display position in the middle of the carbody floor. The calculation results of the rigid–flexible coupled dynamics model established by the uncorrected carbody

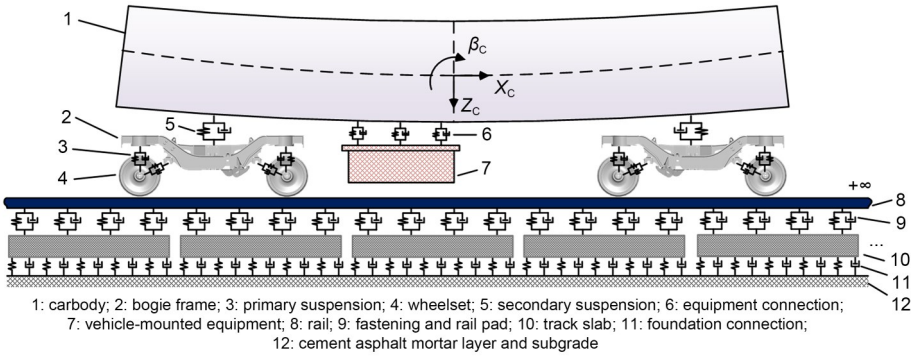

Fig. 13 Schematic view of the high-speed vehicle–track coupled dynamics model. X_C, Z_C, and β_C represent the longitudinal, vertical, and pitching degrees of freedom of the vehicle body, respectively

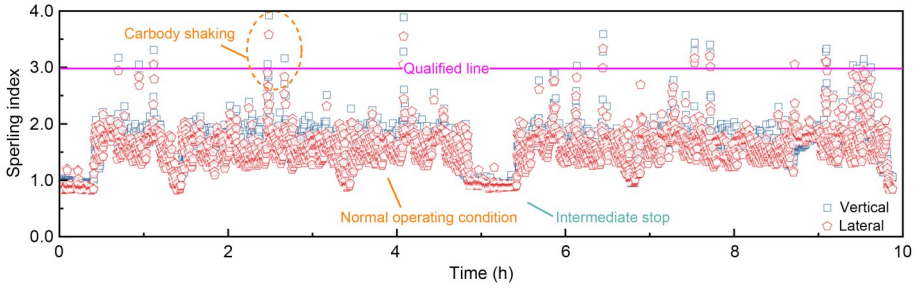

Fig. 14 Sperling index in the middle floor of the vehicle carbody during a certain operation

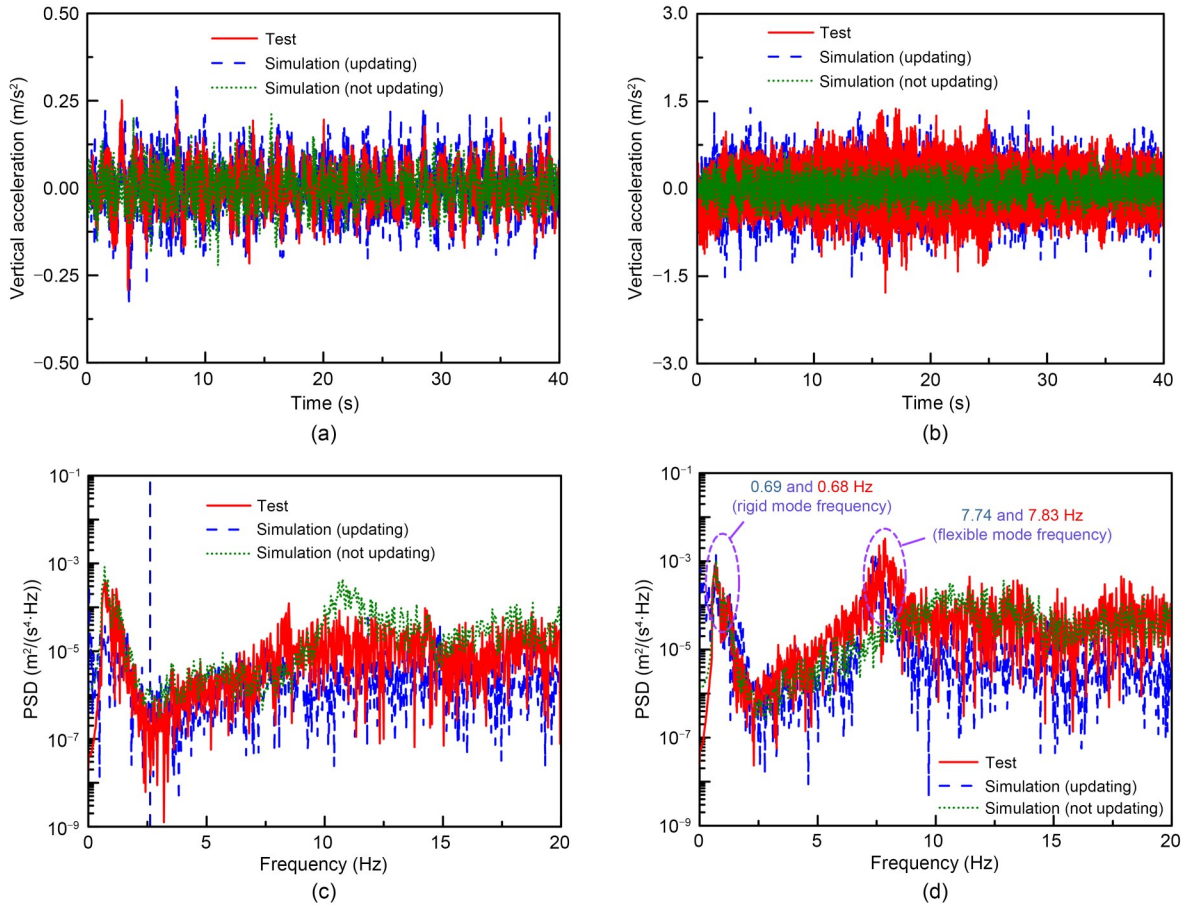

Fig. 15 Vertical acceleration of carbody middle floor under (a) normal operation condition and (b) carbody shaking condition; PSD of carbody middle floor under (c) normal operation condition and (d) carbody shaking condition

FE model are quite different from the test data. Especially under the shaking condition, the fluctuation in the time domain is significantly smaller than the test result. The main reason for this difference is that when the carbody FE model is not updated, the natural frequency is far from the real modal frequency. The accuracy of the modified vehicle rigid–flexible coupled dynamics model was obviously improved.

When carbody shaking appears, the vibration amplitude was about 3–4 times that of normal operation. It can be clearly seen from the PSD that there were obvious acceleration peaks at 0.68 and 7.83 Hz in the frequency domain under the carbody shaking condition. Those frequencies correspond to the rigid body modal frequency and the first-order diamond modal frequency of the carbody, respectively. Because the test and analysis are applied to the vehicle running at high speed, its frequency value is slightly different from the experimental modal frequency (f_1=8.73 Hz) (Orlowitz and Brandt, 2017). The simulation results are in good agreement with the test results and can reproduce the in-situ response characteristics.

6 Conclusions and outlook

The main objective of this paper was to present a method for updating the carbody FE model using measured modal data. To create a comprehensive 3D numerical FE model of an HST carbody in service, different types of FE elements, including beam, shell, mass, and spring-damper, were used. The FE model was optimized and updated based on field modal tests. Numerical results were then used to verify the vertical movement of the carbody floor during specific working conditions of the train operation. Based on these findings, the following conclusions were drawn:

1. The calibration results indicated that the numerical simulation was consistent with the experimental measurements. Compared with the initial carbody FE

model before calibration, the updated carbody FE model showed a significant improvement in the simulation of modal parameters. The frequencies obtained by the updated model deviated slightly from the experimental frequencies, and the MAC indicators increased. The optimization results show that the material property parameters of the four regions of the carbody changed greatly compared with the aluminum alloy material, which is related to the service condition of the carbody

2. The vehicle–track coupled dynamics model was established by using the updated carbody FE model, and the dynamics response of the HST vehicle under normal operation condition and flexible resonance condition was simulated. The simulation results were in good agreement with the measured data, indicating that the updated carbody FE model accurately reflected the actual elastic resonance problem of the HST vehicle in the dynamics analysis.

Future work will focus on using the modified rigid–flexible coupled dynamics model to study how to deal with abnormal vibrations of HSTs, such as installing a dynamic vibration absorber beneath the underframe and bogie active suspension control devices.

Acknowledgments

The authors wish to thank all the staff members involved in the test at the CRRC Changchun Railway Vehicles Co., Ltd., China. This work is supported by the State Key Laboratory of Rail Transit Vehicle System (No. RVL2508), China, the National Natural Science Foundation of China (Nos. 52388102 and U2268210), and the Key Science and Technology Projects of CRRC (No. 2020CYB147), China.

Author contributions

Chao CHANG designed the research and wrote the first draft of the manuscript. Chao CHANG and Xiaoyi MA processed the experimental and numerical data. Fansong LI and Tao LIU helped to organize the manuscript. Liang LING and Wanming ZHAI revised and edited the final version.

Conflict of interest

Chao CHANG, Liang LING, Xiaoyi MA, Fansong LI, Tao LIU, and Wanming ZHAI declare that they have no conflict of interest.

References

Akiyama Y, Tomioka T, Takigami T, et al., 2020. A three-dimensional analytical model and parameter determination method of the elastic vibration of a railway vehicle carbody. *Vehicle System Dynamics*, 58(4):545-568. https://doi.org/10.1080/00423114.2019.1590606

Alkayem NF, Cao MS, Zhang YF, et al., 2018. Structural damage detection using finite element model updating with evolutionary algorithms: a survey. *Neural Computing and Applications*, 30(2):389-411. https://doi.org/10.1007/s00521-017-3284-1

Arora V, 2011. Comparative study of finite element model updating methods. *Journal of Vibration and Control*, 17(13): 2023-2039. https://doi.org/10.1177/1077546310395967

Boo SH, Kim JH, Lee PS, 2018. Towards improving the enhanced Craig–Bampton method. *Computers & Structures*, 196:63-75. https://doi.org/10.1016/j.compstruc.2017.10.017

Bragança C, Neto J, Pinto N, et al., 2022. Calibration and validation of a freight wagon dynamic model in operating conditions based on limited experimental data. *Vehicle System Dynamics*, 60(9):3024–3050. https://doi.org/10.1080/00423114.2021.1933091

Carne TG, Dohrmann CR, 1995. A modal test design strategy for model correlation. Proceedings of the 13th International Modal Analysis Conference, p.927-933.

Chang C, Ding X, Ling L, et al., 2023. Mechanism of high-speed train carbody shaking due to degradation of wheel–rail contact geometry. *International Journal of Rail Transportation*, 11(3):289-316. https://doi.org/10.1080/23248378.2022.2077850

Chen Y, Jing L, Li T, et al., 2023. Numerical study of wheel–rail adhesion performance of new-concept high-speed trains with aerodynamic wings. *Journal of Zhejiang University-SCIENCE A*, 24(8):673-691. https://doi.org/10.1631/jzus.A2300025

Girardi M, Padovani C, Pellegrini D, et al., 2021. A finite element model updating method based on global optimization. *Mechanical Systems and Signal Processing*, 152: 107372. https://doi.org/10.1016/j.ymssp.2020.107372

Gong D, Duan Y, Wang K, et al., 2019. Modelling rubber dynamic stiffness for numerical predictions of the effects of temperature and speed on the vibration of a railway vehicle car body. *Journal of Sound and Vibration*, 449: 121-139. https://doi.org/10.1016/j.jsv.2019.02.037

Helton JC, Davis FJ, 2003. Latin hypercube sampling and the propagation of uncertainty in analyses of complex systems. *Reliability Engineering & System Safety*, 81(1):23-69. https://doi.org/10.1016/S0951-8320(03)00058-9

Huang CH, Zeng J, 2022. Suppression of the flexible carbody resonance due to bogie instability by using a DVA suspended on the bogie frame. *Vehicle System Dynamics*, 60(9): 3051-3070. https://doi.org/10.1080/00423114.2021.1930071

Hu YL, Ge X, Ling L, et al., 2025. Dynamic performance of a high-speed train exiting a tunnel under crosswinds. *Journal of Zhejiang University-SCIENCE A*, 26(1):21-35. https://doi.org//10.1631/jzus.A2300610

Jiang HW, Gao L, Zhao WQ, 2021. Model updating of the vehicle–track coupled system based on in-situ dynamic

measurements. *Construction and Building Materials*, 298: 123861.
https://doi.org/10.1016/j.conbuildmat.2021.123861

Jing L, Wang KY, Zhai WM, 2021. Impact vibration behavior of railway vehicles: a state-of-the-art overview. *Acta Mechanica Sinica*, 37(8):1193-1221.
https://doi.org/10.1007/s10409-021-01140-9

Jung DS, Kim CY, 2013. Finite element model updating on small-scale bridge model using the hybrid genetic algorithm. *Structure and Infrastructure Engineering*, 9(5):481-495.
https://doi.org/10.1080/15732479.2011.564635

Kalker JJ, 1967. On the Rolling Contact of Two Elastic Bodies in the Presence of Dry Friction. PhD Thesis, Delft University, Delft, the Netherlands.

Kalker JJ, 1982. A fast algorithm for the simplified theory of rolling contact. *Vehicle System Dynamics*, 11(1):1-13.
https://doi.org/10.1080/00423118208968684

Li FS, Wu H, Wu PB, 2021. Vibration fatigue dynamic stress simulation under non-stationary state. *Mechanical Systems and Signal Processing*, 146:107006.
https://doi.org/10.1016/j.ymssp.2020.107006

Li FS, Wu H, Liu CT, et al., 2022. Vibration fatigue analysis of high-speed railway vehicle carbody under shaking condition. *Vehicle System Dynamics*, 60(6):1867-1887.
https://doi.org/10.1080/00423114.2021.1880013

Malveiro J, Sousa C, Ribeiro D, et al., 2018. Impact of track irregularities and damping on the fatigue damage of a railway bridge deck slab. *Structure and Infrastructure Engineering*, 14(9):1257-1268.
https://doi.org/10.1080/15732479.2017.1418010

Molodova M, Li ZL, Núñez A, et al., 2014. Validation of a finite element model for axle box acceleration at squats in the high frequency range. *Computers & Structures*, 141:84-93.
https://doi.org/10.1016/j.compstruc.2014.05.005

Montenegro PA, Neves SGM, Calçada R, et al., 2015. Wheel–rail contact formulation for analyzing the lateral train-structure dynamic interaction. *Computers & Structures*, 152:200-214.
https://doi.org/10.1016/j.compstruc.2015.01.004

Orlowitz E, Brandt A, 2017. Comparison of experimental and operational modal analysis on a laboratory test plate. *Measurement*, 102:121-130.
https://doi.org/10.1016/j.measurement.2017.02.001

Paige CC, 1972. Computational variants of the Lanczos method for the eigenproblem. *IMA Journal of Applied Mathematics*, 10(3):373-381.
https://doi.org/10.1093/imamat/10.3.373

Paixão A, Fortunato E, Calçada R, 2014. Transition zones to railway bridges: track measurements and numerical modelling. *Engineering Structures*, 80:435-443.
https://doi.org/10.1016/j.engstruct.2014.09.024

Papadimitriou C, Papadioti DC, 2013. Component mode synthesis techniques for finite element model updating. *Computers & Structures*, 126:15-28.
https://doi.org/10.1016/j.compstruc.2012.10.018

Pedram M, Esfandiari A, Khedmati MR, 2017. Damage detection by a FE model updating method using power spectral density: numerical and experimental investigation. *Journal of Sound and Vibration*, 397:51-76.
https://doi.org/10.1016/j.jsv.2017.02.052

Peeters B, Van der Auweraer H, Guillaume P, et al., 2004. The PolyMAX frequency-domain method: a new standard for modal parameter estimation? *Shock and Vibration*, 11(3-4): 395-409.
https://doi.org/10.1155/2004/523692

Piotrowski J, Kik W, 2008. A simplified model of wheel/rail contact mechanics for non-Hertzian problems and its application in rail vehicle dynamic simulations. *Vehicle System Dynamics*, 46(1-2):27-48.
https://doi.org/10.1080/00423110701586444

Polach O, Nicklisch D, 2016. Wheel/rail contact geometry parameters in regard to vehicle behaviour and their alteration with wear. *Wear*, 366-367:200-208.
https://doi.org/10.1016/j.wear.2016.03.029

Ramancha MK, Astroza R, Madarshahian R, et al., 2022. Bayesian updating and identifiability assessment of nonlinear finite element models. *Mechanical Systems and Signal Processing*, 167:108517.
https://doi.org/10.1016/j.ymssp.2021.108517

Reynders E, Houbrechts J, de Roeck G, 2012. Fully automated (operational) modal analysis. *Mechanical Systems and Signal Processing*, 29:228-250.
https://doi.org/10.1016/j.ymssp.2012.01.007

Rezaiee-Pajand M, Sarmadi H, Entezami A, 2021. A hybrid sensitivity function and Lanczos bidiagonalization–Tikhonov method for structural model updating: application to a full-scale bridge structure. *Applied Mathematical Modelling*, 89:860-884.
https://doi.org/10.1016/j.apm.2020.07.044

Ribeiro D, Calçada R, Delgado R, et al., 2013. Finite-element model calibration of a railway vehicle based on experimental modal parameters. *Vehicle System Dynamics*, 51(6): 821-856.
https://doi.org/10.1080/00423114.2013.778416

Ribeiro D, Calçada R, Brehm M, et al., 2021. Calibration of the numerical model of a track section over a railway bridge based on dynamic tests. *Structures*, 34:4124-4141.
https://doi.org/10.1016/j.istruc.2021.09.109

Ribeiro D, Bragança C, Costa C, et al., 2022. Calibration of the numerical model of a freight railway vehicle based on experimental modal parameters. *Structures*, 38:108-122.
https://doi.org/10.1016/j.istruc.2022.01.085

Sadri M, Brunskog J, Younesian D, 2016. Application of a Bayesian algorithm for the statistical energy model updating of a railway coach. *Applied Acoustics*, 112:84-107.
https://doi.org/10.1016/j.apacoust.2016.05.014

Shi HL, Wu PB, 2016. Flexible vibration analysis for car body of high-speed EMU. *Journal of Mechanical Science and Technology*, 30(1):55-66.
https://doi.org/10.1007/s12206-015-1207-6

Silva R, Ribeiro D, Bragança C, et al., 2021. Model updating of a freight wagon based on dynamic tests under different loading scenarios. *Applied Sciences*, 11(22):10691.
https://doi.org/10.3390/app112210691

Simoen E, de Roeck G, Lombaert G, 2015. Dealing with

uncertainty in model updating for damage assessment: a review. *Mechanical Systems and Signal Processing*, 56-57: 123-149. https://doi.org/10.1016/j.ymssp.2014.11.001

Sun JF, Chi MR, Jin XS, et al., 2021. Experimental and numerical study on carbody hunting of electric locomotive induced by low wheel–rail contact conicity. *Vehicle System Dynamics*, 59(2):203-223. https://doi.org/10.1080/00423114.2019.1674344

Sun Y, Shi FF, Zhang S, et al., 2023. Improving the robustness of non-Hertzian wheel–rail contact model for railway vehicle dynamics simulation. *Multibody System Dynamics*, 59(2):193-237. https://doi.org/10.1007/s11044-023-09903-x

Szafrański M, 2021. A dynamic vehicle–bridge model based on the modal identification results of an existing EN57 train and bridge spans with non-ballasted tracks. *Mechanical Systems and Signal Processing*, 146:107039. https://doi.org/10.1016/j.ymssp.2020.107039

Ticona Melo LR, Ribeiro D, Calçada R, et al., 2020. Validation of a vertical train–track–bridge dynamic interaction model based on limited experimental data. *Structure and Infrastructure Engineering*, 16(1):181-201. https://doi.org/10.1080/15732479.2019.1605394

Tran-Ngoc H, Khatir S, Le-Xuan T, et al., 2022. Finite element model updating of a multispan bridge with a hybrid metaheuristic search algorithm using experimental data from wireless triaxial sensors. *Engineering with Computers*, 38(S3):1865-1883. https://doi.org/10.1007/s00366-021-01307-9

UIC (Union Internationale des Chemins de Fer), 1994. Guidelines for Evaluating Passenger Comfort in Relation to Vibration in Railway Vehicles, UIC 513. National Standards of France, Paris, France.

Wei L, Zeng J, Chi MR, et al., 2017. Carbody elastic vibrations of high-speed vehicles caused by bogie hunting instability. *Vehicle System Dynamics*, 55(9):1321-1342. https://doi.org/10.1080/00423114.2017.1310386

Xiong CB, Lian SD, 2021. Structural damage identification based on improved fruit fly optimization algorithm. *KSCE Journal of Civil Engineering*, 25(3):985-1007. https://doi.org/10.1007/s12205-021-1115-5

You TW, Gong D, Zhou JS, et al., 2022. Frequency response function-based model updating of flexible vehicle body using experiment modal parameter. *Vehicle System Dynamics*, 60(11):3930-3954. https://doi.org/10.1080/00423114.2021.1983182

Zhai WM, 2019. Vehicle–Track Coupled Dynamics: Theory and Applications. Springer, Singapore. https://doi.org/10.1007/978-981-32-9283-3

Zhang XY, Jin XL, Qi WG, et al., 2008. Vehicle crash accident reconstruction based on the analysis 3D deformation of the auto-body. *Advances in Engineering Software*, 39(6): 459-465. https://doi.org/10.1016/j.advengsoft.2007.05.002

Zhu HP, Li JJ, Tian W, et al., 2021. An enhanced substructure-based response sensitivity method for finite element model updating of large-scale structures. *Mechanical Systems and Signal Processing*, 154:107359. https://doi.org/10.1016/j.ymssp.2020.107359